Chemical Papers (2020) 74:4253–4265
https://doi.org/10.1007/s11696-020-01244-9

ORIGINAL PAPER

Biogenic synthesis, antioxidant and antimicrobial activity of silver and manganese dioxide nanoparticles using *Cussonia zuluensis* Strey

Nomfundo T. Mahlangeni[1] · Judie Magura[1] · Roshila Moodley[1] · Himansu Baijnath[2] · Hafizah Chenia[2]

Received: 24 January 2020 / Accepted: 4 June 2020 / Published online: 9 June 2020

Abstract

Synthesis of nanoparticles using naturally occurring biomolecules has become the preferred method due to increased concerns over environmental degradation. In this study, the biosynthesis of manganese dioxide nanoparticles (MnO_2NPs) and silver nanoparticles (AgNPs) using extracts and the biomolecule, aralia cerebroside, isolated from the medicinal plant species, *Cussonia zuluensis* Strey, was investigated. The size and morphology of nanoparticles observed using microscopic techniques indicated an average particle size of 7.43 nm (spherical and polydispersed) for AgNPs and a layer of thin film surrounding the particles, confirming the capping by biomolecules. AgNPs exhibited better antibacterial activity than MnO_2NPs and were most active against *Escherichia coli* and *Enterococcus faecalis*. MnO_2NPs presented as ultrathin nanoflakes with grainy morphology ranging from 11 to 29 nm when capped with biomolecules from the extract, and presented as nanospheres surrounded by nanosheets ranging from 6.99 to 16.57 nm when capped with aralia cerebroside. The radical scavenging activity was found to be MnO_2NPs (extract) > MnO_2NPs (cerebroside) > AgNPs (extract) > extract > cerebroside, and the ferric reducing antioxidant power was found to be cerebroside > extract > MnO_2NPs (cerebroside) > MnO_2NPs (extract) > AgNPs (extract). MnO_2NPs exhibited better antioxidant activity than AgNPs with size and morphology of nanoparticles being influenced by the capping agent, which, in turn, influenced antioxidant activity as seen with MnO_2NPs. This study confirms the significance of the metal or metal oxide core and capping biomolecules for targeted therapeutic activity of nanoparticles using the plant-mediated synthesis route.

Keywords Aralia cerebroside · Silver nanoparticles · Radical scavenging activity · *Escherichia coli* · *Enterococcus faecalis*

Introduction

The synthesis of nanoparticles using biological materials has been proposed to be a non-toxic and eco-friendly alternative to physical and chemical approaches (Parveen et al. 2016; Nasrollahzadeh et al. 2019). The biological materials including DNA, proteins, peptides, bacteria, fungus and plants have been successfully exploited for the synthesis of nanoparticles (Deljou and Goudarzi 2016; Leng et al. 2016; Corra et al. 2017; Julin et al. 2018; Shen et al. 2018; Demirbas et al. 2019; Guilger-Casagrande et al. 2019). However, plants and plant-derived extracts have gained substantially more interest due to availability, cost-effectiveness and ease of use for large-scale synthesis (Hazarika et al. 2017). Moreover, well-characterized and stable nanoparticles have been reported to have been synthesized using plants more than other organisms (Iravani 2011; Ahmed et al. 2016; Demirbas et al. 2019; Some et al. 2019). Plants are enriched with various bioactive metabolites such as terpenoids, alkaloids, flavonoids, sugars, proteins and steroids that act as reducing and stabilizing agents during nanoparticle synthesis (Makarov et al. 2014; Ocsy et al. 2017).

Metal nanoparticles have gained popularity over the years, with silver nanoparticles (AgNPs) being widely used due to potential antimicrobial, anti-inflammatory and antifungal activities (Elgorban et al. 2016; Kedi et al. 2018). The reducing agent used for the synthesis of AGNPs influences

Electronic supplementary material The online version of this article (https://doi.org/10.1007/s11696-020-01244-9) contains supplementary material, which is available to authorized users.

✉ Roshila Moodley
moodleyrosh@ukzn.ac.za

[1] School of Chemistry and Physics, University of KwaZulu-Natal, Durban 4000, South Africa

[2] School of Life Sciences, University of KwaZulu-Natal, Durban 4000, South Africa

their size, shape, surface chemistry and agglomeration, which influences their biological activity (Singh and Kaur 2019). Several studies have been reported on the green synthesis of AgNPs using plants and their enhanced antimicrobial activity (Dogru et al. 2017; Loo et al. 2018; Sana and Dogiparthi 2018).

Manganese dioxide (MnO_2) is reported to be one of the most attractive inorganic materials among the studied metals in nanotechnology, imparting both photocatalytic and antimicrobial actions (Moon et al. 2015; Hoseinpour et al. 2018; Joshi et al. 2020). This is mainly due to its extensive chemical and physical properties as well as its vast range of applications in ion exchange, energy storage, imaging contrast and medicine (Jaganyi et al. 2013; Haneefa et al. 2017). Previous studies have reported on the successful synthesis of MnO_2 using chemical and physical methods (Moon et al. 2013; Kumar et al. 2014; Cherian et al. 2016), as well as the plant-mediated synthesis route, which was found to be cost-effective and eco-friendly, and allowed for ease of synthesis at room temperature and pressure, and optimization of size and shape (Malik et al. 2014).

In this study, we report on the green synthesis of Ag and MnO_2 nanoparticles using *Cussonia zuluensis* for the first time. The *Cussonia* genus, commonly known as the "cabbage tree," belongs to the family *Araliaceae*. It is widely distributed in the southern Cape and eastern parts of South Africa, extending to Zimbabwe, Zambia and Mozambique (Hankey 2005). Traditionally, *Cussonia* is used to treat malaria, sexually transmitted infections, wounds, skin rashes, rheumatism and cancer (Nitie-Kang et al. 2014; Oladimeji et al. 2017). *Cussonia* species have also been reported to possess potent antimicrobial and antimalarial activity (De Villiers et al. 2010), immunomodulatory activities (Oladimeji et al. 2017) and antibacterial activity against *Staphylococcus aureus* (Tetyana et al. 2002). However, to the best of our knowledge, there have been no scientific reports on the phytochemical constituents or biological activity of *C. zuluensis*. Herein, we report also on the synthesis of AgNPs and MnO_2NPs using the crude methanol extracts and isolates from *C. zuluensis* and their antimicrobial and antioxidant activities. The aim of this study was to determine the effects of the metal or metal oxide core and biosynthesizing agents on particle characteristics and to evaluate the combined synergistic or antagonistic effects of the biomolecules and nanoparticles on biological activity.

Materials and methods

Fresh storm uprooted tubers of *C. zuluensis* were collected from Durban, South Africa. A voucher specimen (Magura J2) was deposited in the ward herbarium, School of Life Science (UKZN). Initially the samples (1.3 kg) were washed with double distilled water, air-dried and ground using a mortar and pestle prior to analysis. NMR deuterated solvents, potassium permanganate ($KMnO_4$), silver nitrate ($AgNO_3$), Mueller–Hinton agar, antibiotic disks and all organic solvents used for extraction were supplied by Sigma-Aldrich, Germany. Cultures for antimicrobial activity were procured from the American Type Culture Collection (ATCC), Manassas, Virginia, USA.

Extraction, isolation and characterization of compounds

The ground plant material was exhaustively extracted with methanol (MeOH) for 72 h, the extracts of which were concentrated using a rotary evaporator and dissolved in 300 mL of water. The aqueous mixture was further portioned with dichloromethane (DCM) followed by ethyl acetate (EtOAc) in equal volumes. The obtained DCM fraction (12.5 g) and EtOAc fraction (4.2 g) were separately subjected to column chromatography using silica gel (Merck Kieselgel 60, 0.063–0.200 mm, 70–230 mesh ASTM). The columns were eluted using a step gradient (hexane: EtOAc) starting with 100% hexane that was stepped by 10% to 100% EtOAc. The collected fractions were monitored by thin-layer chromatography (TLC) (Merck silica gel 60, 20 × 20 cm F_{254} aluminum sheets), and fractions with similar TLC profiles were combined and crystallized. Fractions 16–20 from the DCM fraction afforded the isolation of compound 1 (25 mg) as a white solid. Fractions 30–33 from the DCM fraction gave compound 2 (11 mg). The elution of the EtOAc fraction using hexane: EtOAc (6:4) solvent system yielded compound 3 (60 mg) as a yellow powder and compound 4 (100 mg).

Aralia cerebroside (4): off white solid, UV λmax(MeOH): 213, 255, 289 nm; IR ν_{max} 3231(OH), 2912, 2852 (CH), 1541 (NH), 1070, 1030 (C-O glucose), 719 ($(CH_2)_n$); ^{1}H-NMR (400 MHz, CD_3OD) δ7.76 (1H, *d*, *J* = 9.9 Hz, NH), 5.34 (1H, *dt*, *J* = 5.4, 11.1 Hz, H-9), 5.29 (1H, *dt*, *J* = 5.4, 11.1 Hz, H-8), 4.22 (1 H, *d*, *J* = 7.7 Hz, H–l"), 4.19 (1H, *m*, H-2), 4.00 (1H, *m*, H-lb), 3.96 (1H, m, H-4), 3.78 (1H, *dd*, J = 1.4,12.9 Hz, H-6"b), 3.74(1H, *m*, H-la), 3.63(1H, *m*, H-3), 3.61 (1H, *dd*, *J* = 3.3, 12.9 Hz, H6″a), 3.53 (1H, *m*, H-2′), 3.29 (1H, *m*, H-3″, 4″), 3.21 (1H, *m*, H-5″), 3.12 (1H, *d*, *J* = 8.9 Hz, H-2″), 1.97 (2H, *m*, H-5), 1.90 (2H, *m*, H-7), 1.66 (2H, *m*, H-3′b), 1.55 (4H, *m*, H-10, 3′a), 1.33 (2H, *m*, H-4′), 1.26-1.21 [*brs*,(CH_2)n, 11-17, 5′-15′], 0.82 (6H, *t*-like, *J* = 6.7 Hz, H-18, 16′); ^{13}C-NMR (400 MHz, CD_3OD) δ177.1 (C-1′), 130.9 (C-9), 130.7 (C-8), 104.6(C-1″), 78.0 (C-5″), 77.8 (C-3″), 75.5 (C-3), 75.0 (C-2″), 73.0 (C-4, 2′), 71.5 (C-4″), 69.9 (C-1), 62.6 (C-6″), 51.6 (C-2), 35.7 (C-3′), 33.8 (C-7), 33.7 (C-4′), 33.1 (C-10), 30.5 (C-4′), 28.4(C-5), 28.3 (C-6), 30.8-23.7 (C-6, 11-17, 5′-15′), 14.4 (C-18, 16′); LC–MS *m/z* 733 $[M+2H]^+$, 570 $[M+2H - 162]^+$; positive

TOF–MS *m/z* 754 $[M+Na]^+$; 553 $[M+Na\text{-}C_6H_{10}O_6]^+$, 310 $[M+Na\text{-}C_6H_{10}O_6\text{-}243)]^+$, 239 $[M+Na\text{-}C_6H_{10}O_6\text{-}243\text{-}71)]^+$.

Nuclear magnetic resonance (NMR) spectra were recorded on a Bruker Advance III 400 MHz spectrometer (Germany) using deuterated chloroform ($CDCl_3$), dimethyl sulfoxide (DMSO) or methanol (CD_3OD) (Merck, Germany). Fourier transform infrared (FT-IR) spectra were recorded on a PerkinElmer Universal ATR spectrometer (USA). Liquid chromatography–mass spectrometry (LC–MS) data were obtained using an Agilent LC-MSD apparatus (USA) equipped with a UV detector using a mobile phase of 95% acetonitrile, 10% water and both containing 1.1% formic acid at a flow rate of 1 mL min^{-1}. Low-resolution mass spectrometry was done on a Waters Micromass LCT Premier TOF–MS instrument (USA).

Green synthesis of Ag nanoparticles

About 10 g of dried and crushed plant material was extracted with 100 mL of MeOH using an orbital shaker at room temperature then filtered. The filtrate (50 mL) was used for the synthesis of AgNPs by adding to 100 mL of 50 mM $AgNO_3$ (the only concentration that resulted in NP formation from preliminary tests) dropwise, at room temperature. The mixture was left to stand for 24 h.

Green synthesis of MnO_2 nanoparticles

The filtrate from the MeOH extract of *C. zuluensis* and compound 4 were used for the synthesis of MnO_2 nanoparticles. A 50 mL aliquot of the filtrate was added dropwise to 100 mL of freshly prepared 10 mM $KMnO_4$ solution (the concentration that produced smaller NPs and gave a better yield from preliminary tests) at room temperature which was left to stand for 24 h. A color change from purple to dark brown indicated the formation of the nanoparticles. For the synthesis of nanoparticles using compound 4, 10 mg of the compound was dissolved in 10 mL of MeOH and reacted with 20 mL of 10 mM $KMnO_4$ for 24 h standing.

Characterization of the synthesized nanoparticles

The synthesized nanoparticles were purified by centrifugation at 5000 rpm for 30 min and washed three times with double distilled water. The purified pellet was oven-dried at 60 °C to form a powder. The formation of the nanoparticles was confirmed by UV–Vis spectroscopy (Shimadzu UV-1800 spectrophotometer, Japan) and FT-IR. The size and morphology of the nanoparticles were obtained by high-resolution transmission electron microscopy (HRTEM) images using a JEOL 2100 operated at a voltage of 200 kV, and a drop of the reaction mixture was loaded on the copper grid and allowed to evaporate under infrared light. SEM measurements were taken on the ultra plus field emission scanning electron microscope (FESEM) (Carl Zeiss, Germany) with accelerating voltage of 5 kV. Elemental composition of the nanoparticles was obtained using FESEM and analyzed using electron-dispersive X-ray (EDX) (Aztec Analysis Software, England). Selected area electron diffraction (SAED) was obtained on the HRTEM to examine the crystallinity of the nanoparticles.

Antimicrobial activity

The antimicrobial activity of AgNPs and MnO_2NPs was tested against human pathogenic *Enterococcus faecalis* ATCC 29212, *Escherichia coli* ATCC 35218, ATCC 25922, *Klebsiella pneumonia* ATCC 700603 and *Staphylococcus aureus* ATCC 43300 and ATCC 29213, using the standard well diffusion method. Mueller–Hinton (MH) agar media were used to culture bacterial strains at 37 °C, overnight. Freshly cultured bacterial strains were spread onto the Mueller–Hinton agar plates, and the wells were prepared using a 3 mm sterile borer. Aliquots of 20 µL and 40 µL of the AgNPs prepared with crude extract and MnO_2NPs prepared with the crude extract or phytocompound and distilled water (negative control) were added to the wells and incubated at 37 °C, overnight. Ampicillin disks served as a positive control (10 µg per disk), and the antimicrobial activity was measured based on the average diameter (mm) of the inhibition zone around the wells.

Antioxidant activity

DPPH assay

The filtrate from the MeOH extract of *C. zuluensis* and compound 4 were used for the synthesis of MnO_2 nanoparticles. A 50 mL aliquot of the filtrate was added dropwise to 100 mL of freshly prepared 10 mM $KMnO_4$ solution at room temperature which was left to stand for 24 h. A color change from purple to dark brown indicated the formation of the nanoparticles. For the synthesis of nanoparticles using compound 4, 10 mg of the compound was dissolved in 10 mL of MeOH and reacted with 20 mL of 10 mM $KMnO_4$ for 24 h standing. Percentage inhibition is calculated using Eq. (1):

$$\%\ \text{Inhibition} = \left(\frac{A_C - A_S}{A_C}\right)\text{x}100 \quad (1)$$

where A_c was the absorbance of the control and A_s was the absorbance of samples

Ferric reducing power assay

The reducing power of the plant extract, compound, nanoparticles or standard (ascorbic acid, α-tocopherol and BHT) was determined as described previously (Sangaonkar and

Pawar 2018). The absorbance was then measured at 700 nm against a blank using a UV–Vis spectrophotometer (VWR UV-1600 PC spectrophotometer, Leicestershire, UK).

Phosphomolybdenum assay

The total antioxidant activity of plant extract, compound, nanoparticles or standard (ascorbic acid, α-tocopherol and BHT) was measured as described previously (Saeed et al. 2012). The absorbance was measured at 765 nm against a blank using a UV–Vis spectrophotometer.

Statistical analysis

The results were expressed as mean ± standard deviation of three independent experiments. One-way analysis of variance (ANOVA) was performed on the data to evaluate significant difference between means followed by Tukey's post hoc test ($p < 0.05$). All statistical analyses were performed using GraphPad Prism 5.0 (GraphPad Software Inc., San Diego, CA).

Results and discussion

Isolated compounds

Phytochemical analysis of *C. zuluensis* yielded compound 1 as white crystals with a molecular ion peak at *m/z* 393 $[M-(H_2O+H)]^+$. The ^{1}H NMR spectrum showed characteristic peaks at δ_H 5.02, 5.12 and 5.32 correlating with carbon resonances at δ_C 129.2, 138.3 and 121.7, respectively, in the HSQC spectrum (Fig. S1a–S1e). The spectroscopic data were consistent with that in the literature for stigmasterol (Ahmed et al. 2013).

Compound 2 was isolated as a mixture with molecular ion peaks at *m/z* 138 and 168 obtained by LC–MS corresponding to the molecular formulae of $C_7H_6O_3$ and $C_8H_8O_4$, respectively. The ^{1}H NMR spectrum indicated a 1,4-disusbstituted benzene ring with resonances at δ_H 6.95 (2H, *d*, $J = 8.3$ Hz, H-3, 5) and 7.99 (2H, *d*, $J = 8.3$ Hz, H-2, 6) for compound 2A, and a 1,3,4-trisubstituted benzene ring with resonances at δ_H 6.86 (1H, *d*, $J = 8.4$ Hz, H-5), 7.56 (1H, *d*, $J = 1.9$ Hz, H-2) and 7.69 (1H, *dd*, $J = 1.9$, 8.4 Hz, H-6) for compound 2B. The carbon resonance at δ_C 170.5 in the ^{13}C NMR spectrum (Fig. S2a–S2i) was attributed to the carbonyl that was overlapping for both compounds. Two characteristic absorption peaks at 256 nm and 289 nm in the UV–Vis spectrum were due to the non-symmetrical structure of compound 2B; the intensity of the peak at 256 nm suggested the overlap of peaks for the symmetrical compound 2A. Compound 2 was identified as a mixture of *p*-hydroxybenzoic acid (2A) and 4-hydroxy-3-methoxybenzoic acid (2B) (vanillic acid) by comparison of spectroscopic data with that in the literature (Lee et al. 2013).

Compound 3 was isolated as a white powder with molecular formula of $C_{35}H_{58}O_6$. The ^{1}H NMR spectrum was similar to that of stigmasterol with the exception of a characteristic anomeric proton resonance at δ_H 4.22 (1H, *d*, $J = 7.7$ Hz, H-1′) and resonance at δ_H 2.89–3.14 (sugar). This sugar moiety was confirmed to be attached to C-3 of the aglycone using HMBC correlations (Fig. S3a–S3i). Compound 3 was confirmed to be stigmasterol-3-O-β-D-glucopyranoside (Khatun et al. 2012).

The ^{1}H NMR spectrum showed two single-proton resonances at δ_H 5.34 (1H, *dt*, $J = 7.7$, 11.1 Hz) and 5.29 (1H, *dt*, $J = 7.7$, 11.1 Hz) which were assigned to H-8 and H-9 due to one olefinic bond. The doublet at δ_H 4.22 ($J = 7.7$ Hz) was attributed to the anomeric proton (H-1″) of the sugar moiety. The ^{13}C NMR spectrum showed resonances at δ_C 104.6, 75.0, 77.8, 78.0, 71.5 and 62.6, confirming the presence of the sugar moiety. The ^{1}H and ^{13}C NMR spectra also showed an amide linkage at δ_H 7.76 (*d*, $J = 9.9$ Hz), an amidomethine at δ_H 4.19 (δ_C 51.6, C-2), oxygenated methylene carbons at δ_H 4.00 and 3.74 (δ_C 69.9, C-1) and oxygenated methines at δ_C 75.5 (C-3) and 73.0 (C-4 and 2′). The coupling constant of H-8 and H-9 ($J = 11.1$ Hz) and the chemical shifts of C-7 (δ_C 33.8) and C-10 (δ_C 33.1), next to the double bond, suggested a trans (*E*) configuration (Ling et al. 2006; Zheng et al. 2009; Ebede et al. 2019). The triplet at δ_H 0.82 (6H) that integrated to 6 protons was due to the terminal C-18 and C-16′ primary methyl protons. Based on these results, compound 4 was identified as 1-*O*-β-D-glucopyranosy-(2*S*,3*S*,4-*R*,8*E*)-2-[(2′*R*)-2′-hydroxypalmitoylamino]-8-octadecene-l,3,4-triol, commonly known as aralia cerebroside (Fig. 1) (Kang et al. 1999). This compound has previously been isolated from *Aralia elata* of the Araliaceae family. This is the first report of its isolation from the *Cussonia* genus.

Characterization of Ag and MnO_2 nanoparticles synthesized using the plant extract

The successful reduction of $KMnO_4$ was evidenced by a color change from purple to brown within 30 min of the reaction after the addition of the plant extract. A plausible mechanism for the formation of MnO_2NPs is presented in Fig. 2. An oxidation–reduction reaction initiated by $KMnO_4$ (a strong oxidizing agent that cleaves the alkenes) produces glycols and MnO_2. Potassium permanganate can further oxidize hydroxyl groups into ketones, aldehydes or carboxylic acids (Shaabani et al. 2005). The hydroxyl and carboxyl groups from the plant extract are then adsorbed onto the surface of the MnO_2NPs. The formation of AgNPs and MnO_2NPs was monitored by UV–Vis and IR spectroscopy (Fig. 3). UV–Vis analysis of MnO_2NPs showed a broad peak in the 292–368 nm range characteristic of the surface

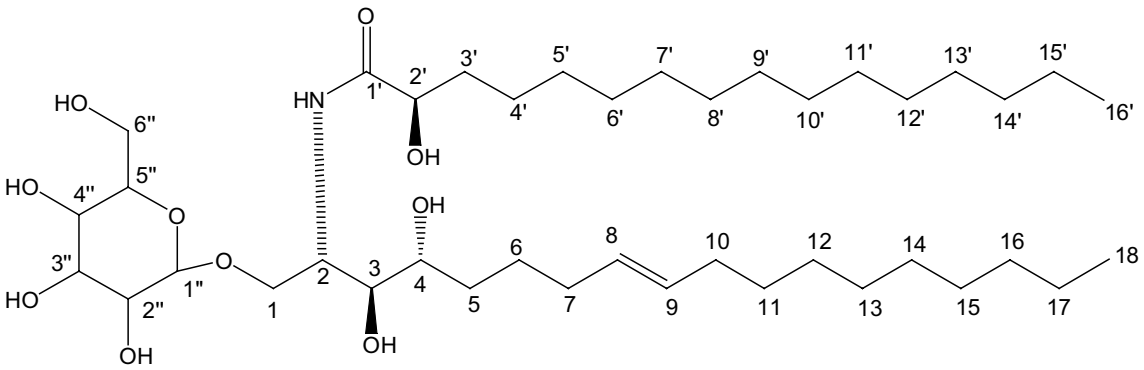

Fig. 1 Structure of isolated compound, aralia cerebroside

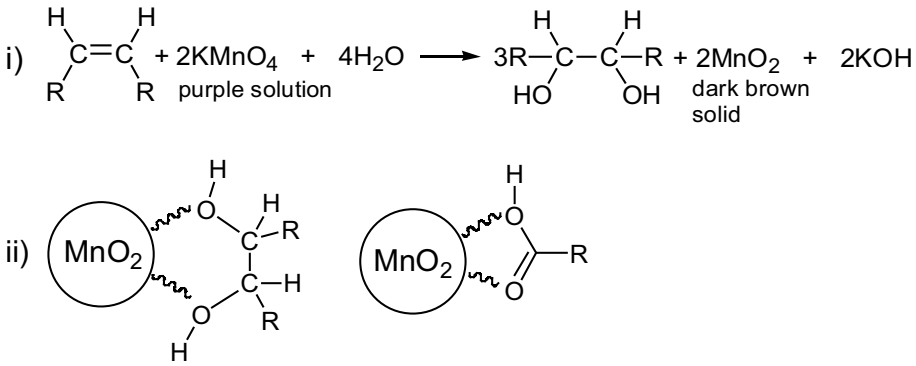

Fig. 2 **a** Plausible mechanism for the formation of MnO_2NPs and **b** illustration of the adsorption of hydroxyl and carboxylic groups onto MnO_2NPs

plasmon resonance (SPR) for MnO_2NPs (360–404 nm) (Luo 2007). Peak broadness indicated aggregation of synthesized MnO_2NPs. The FT-IR spectrum confirmed the presence of MnO_2NPs with an absorption band at 496 cm^{-1} characteristic of O–Mn–O stretching (Wang et al. 2007; Athar et al. 2012). Absorption bands observed at 3360 (O–H stretching), 1581 (C = C aromatic stretching), 1320 (C–O–C stretching) and 1054 cm^{-1} (C–OH stretching) were due to the functional groups present in the extract including benzoic acids, stigmasterol and stigmasterol-3-O-β-D-glucopyranoside, capping the MnO_2NPs. The IR spectra of the extract of *C. zuluensis* and MnO_2NPs showed the disappearance of absorption bands at 716 and 800 cm^{-1} (aromatic C–H out of plane bend) as well as 2862 and 2927 cm^{-1} (CH_2 stretching) for MnO_2NPs, suggesting coordinative interactions between the molecules (benzoic acids, sterols and aralia cerebrosides) and MnO_2NPs (Hazarika et al. 2017).

The AgNPs were obtained by using the extract of *C. zuluensis* as a reducing and stabilizing agent. The solution changed from yellow to cloudy immediately after the addition of $AgNO_3$ with the formation of small yellowish brown particles of AgNPs. The shape, width and shift of the UV–Vis bands indicated its particle size, with shorter wavelengths (blueshift) signifying smaller particles. A broad peak at 301 nm was observed, which was slightly lower than previously reported SPRs for AgNPs (Kaczmarek et al. 2016; Khan et al. 2018). Previous studies indicate that UV absorptions between 300 and 400 nm are due to oxidative dissolution of AgNPs in the aqueous solution (Loza and Epple 2018). Other techniques such as IR, EDX and SAED were employed to further confirm the synthesis of AgNPs. The IR spectrum indicated the disappearance of the O–H (3360 cm^{-1}) and C–O (1025 cm^{-1}) stretching bands for AgNPs. This could be due to the reaction of compounds in *C. zuluensis* containing hydroxyl and phenolic groups with Ag^+ ions, leading to the formation and stabilization of AgNPs. Absorbance bands at 2927–2862 cm^{-1} (CH_2 stretching), 1283 cm^{-1} (C–O–C stretching) and 800–716 cm^{-1} (aromatic C–H out of plane bend) can be attributed to the compounds in *C. zuluensis* capping the AgNPs.

The HRTEM and SEM images, and SAED patterns of AgNPs and MnO_2NPs synthesized using the plant extract as well as the particle size distribution histogram of AgNPs are shown in Fig. 4. The size and morphology of MnO_2NPs examined through HRTEM revealed a layered flake shape morphology that forms an interconnected network (Fig. 4a and b). SEM images confirmed the presence of ultrathin nanoflakes as shown by a grainy morphology from the top view, with a diameter ranging from 11 to 29 nm (Fig. 4c). The basic building block of

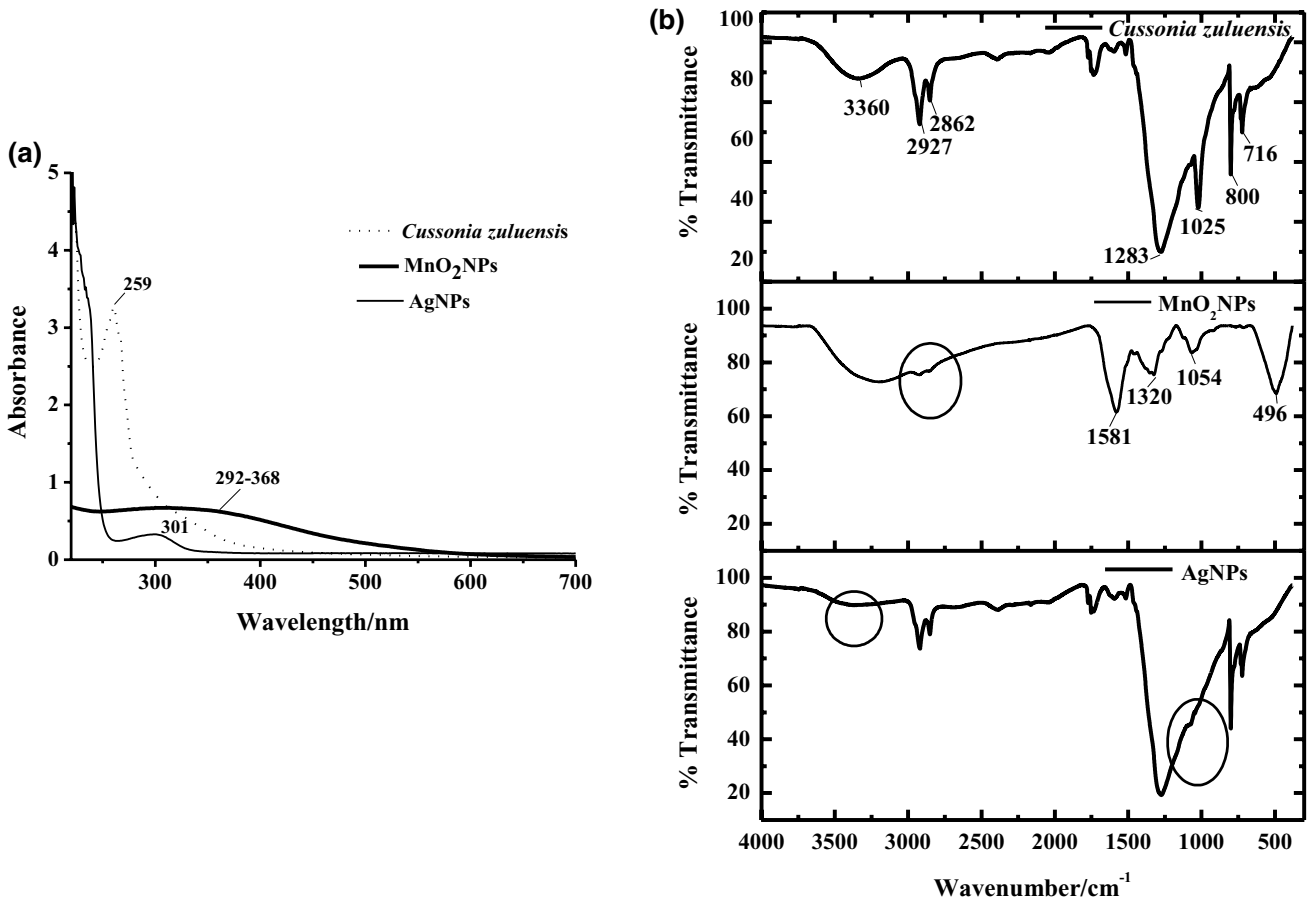

Fig. 3 **a** UV–Vis spectra and **b** IR spectra of *C. zuluensis*, MnO_2NPs and AgNPs synthesized using the plant extract

all phases of MnO_6 octahedra shares edges and corners to form tunneled layers or structures (Birgisson et al. 2018). The compounds in *C. zuluensis* capped the outer layers of MnO_2NPs, thereby resulting in blurry HRTEM images. The SAED pattern for MnO_2NPs displayed continuous rings that were indicated poor crystallinity (Fig. 3b inset). The characteristic interplanar spacing of 0.255 nm (301) and 0.213 nm (202) was attributed to R-MnO_2 (ramsdellite) (Zhai et al. 2013). Ramsdellite contains MnO_6 octahedra connected at the edges to form a 2×1 channel.

The HRTEM image of AgNPs (Fig. 4d) showed spheres that were polydispersed with a particle size range of 2.35–23.98 nm and average size of 7.43 nm, and a layer of thin film surrounding the AgNPs, confirming the capping by phytocompounds. After nucleation of Ag atoms, the nuclei aggregate to form small nanoparticles that rapidly aggregate to form larger nanoparticles, leading to polydispersion (Seoudi et al. 2011). The SEM image indicated the particles to be spherical in nature (Fig. 4f). The SAED pattern for AgNPs showed intense concentric circles with interplanar spacing of 0.23 nm (111) and 0.19 nm (200), which can be attributed to the face centered cubic structure of AgNPs (Fig. 4d inset).

The EDX spectra of MnO_2NPs and AgNPs are presented in Fig. 5 with MnO_2NPs showing an intense Mn signal at 5.9 keV (42%). Signals of oxygen (0.5 keV, 35%) and carbon (0.3 keV, 16%) were due to the compounds present in the plant extract that capped the MnO_2NPs. The potassium signal was attributed to the $KMnO_4$ salt which was used in the synthesis. The copper signal for all EDX spectra was from the copper stub used in sample mounting. The EDX spectrum of AgNPs showed an intense Ag signal (3.1 keV, 39%), confirming the presence of Ag; the carbon (33%) and oxygen (21%) signals were from the extract and the nitrogen (0.4 keV) signal was from the $AgNO_3$ salt, which was used in the synthesis.

Characterization of MnO_2 nanoparticles synthesized with cerebroside

The UV–Vis and IR spectra of MnO_2NPs (cerebroside) are shown in Fig. 6. The formation of MnO_2NPs (cerebroside)

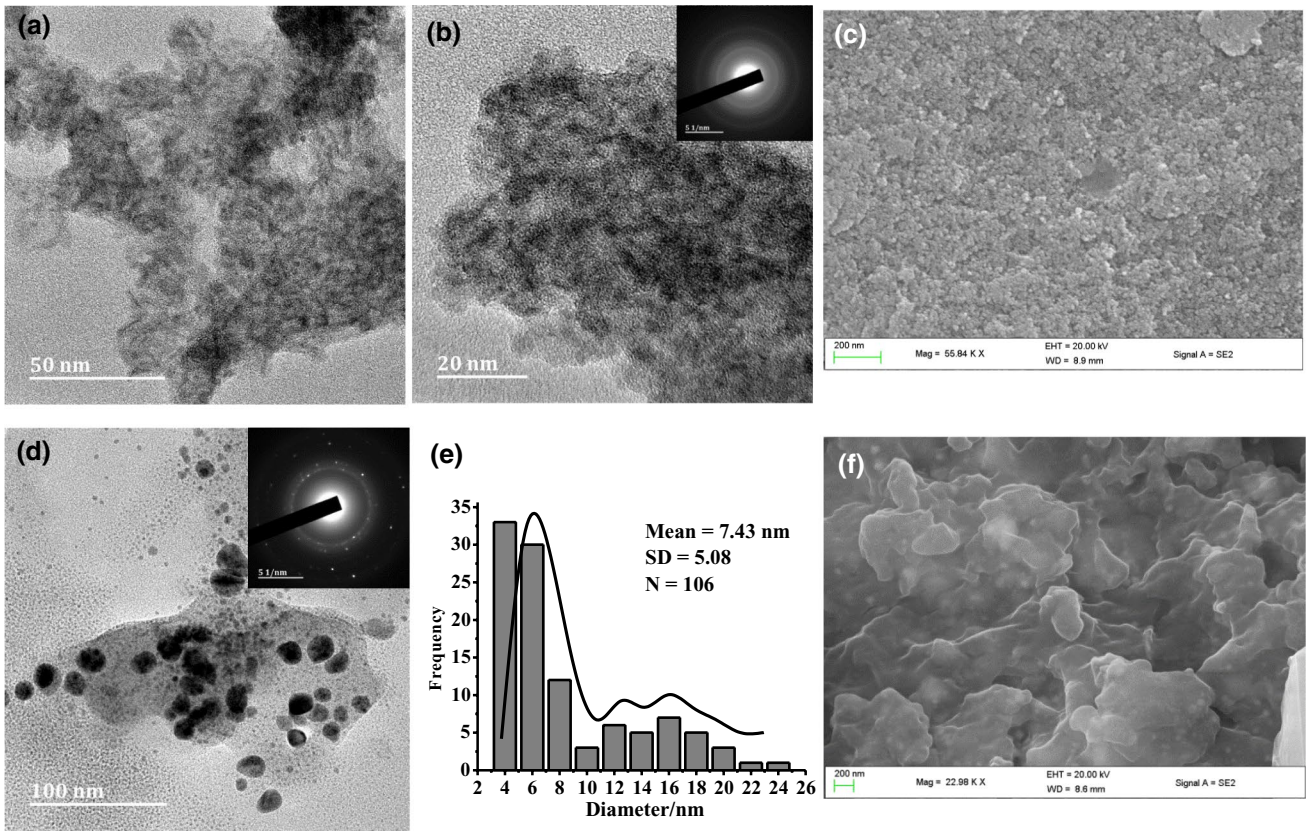

Fig. 4 HRTEM images (**a** and **b** MnO_2NPs; **d** AgNPs) with corresponding SAED patterns (inset), SEM images (**c** MnO_2NPs; **f** AgNPs) and particle distribution histogram (**e** AgNPs) of synthesized nanoparticles using the plant extract

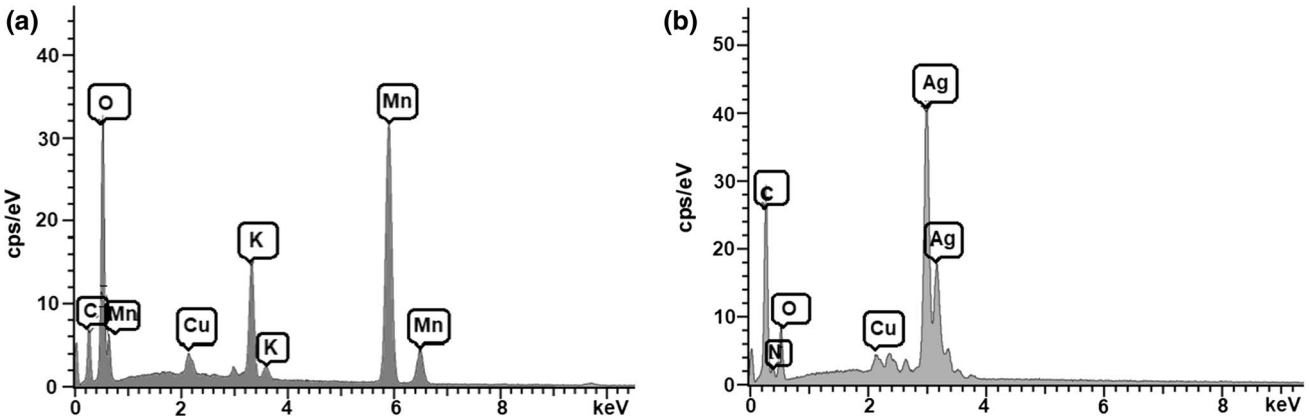

Fig. 5 EDX spectra of **a** MnO_2NPs and **b** AgNPs synthesized using the plant extract

by UV–Vis was observed by the appearance of absorbance peaks at 321–383 nm (Fig. 6a) (Luo 2007). The UV–Vis absorbance range incorporates the characteristic peak of 374 nm for single-layered MnO_2 nanosheets (Liu et al. 2015). The IR spectrum showed bands at 476 and 596 cm^{-1}, which are due to O-Mn stretching and Mn–O–Mn vibrations in the MnO_6 octahedral framework, confirming the formation of MnO_2NPs (cerebroside) (Fig. 6b) (Bayoudh et al. 2016). The IR absorbance bands at 3937 cm^{-1} (O–H stretching), 2922–2851 cm^{-1} (CH_2 stretching), 1578 cm^{-1} (C = C stretching), 1424 cm^{-1} (methyl C–H bending) and 1042 cm^{-1} (C–O stretching) were due to cerebroside coating the NPs. The shift in the wave numbers for C = C stretching (from 1615

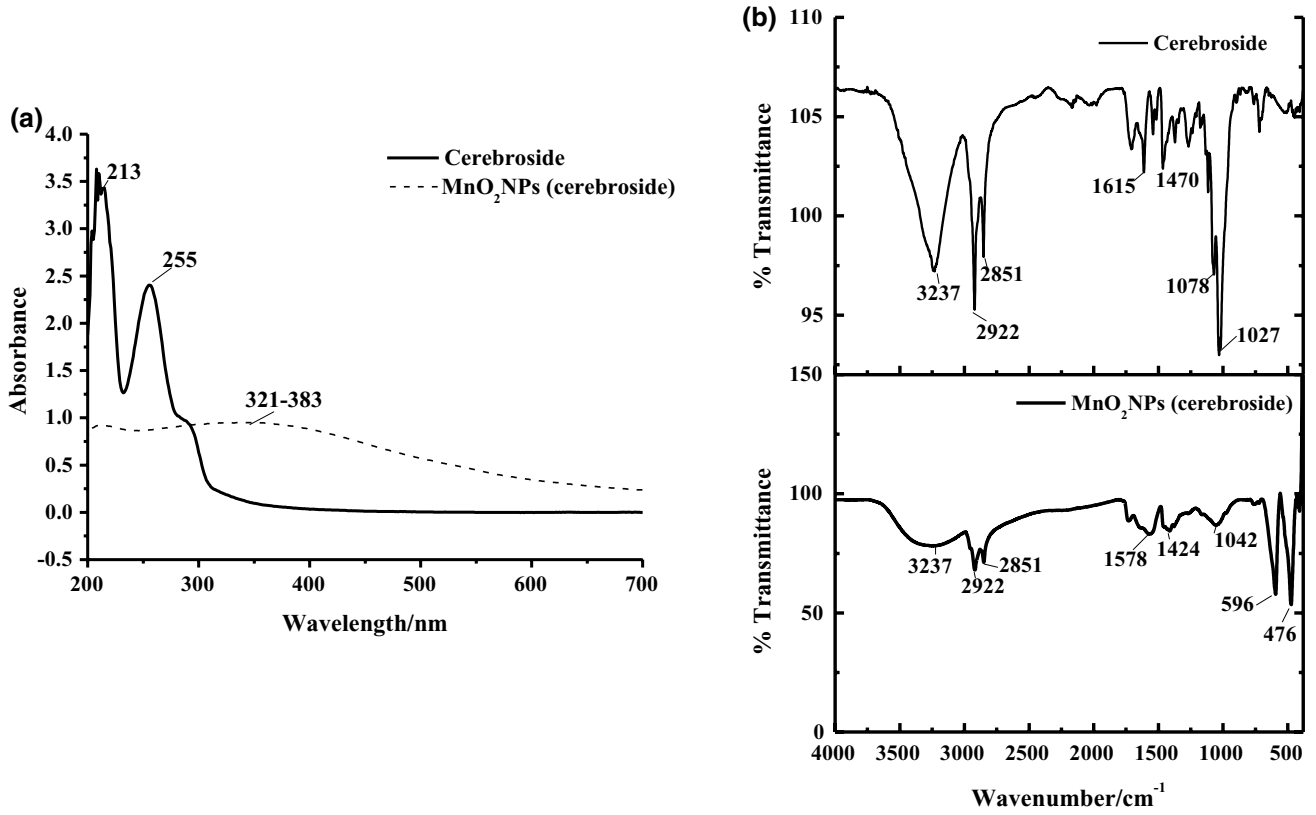

Fig. 6 **a** UV–Vis spectra and **b** IR spectra of cerebroside and MnO_2NPs (cerebroside)

to 1578 cm^{-1}), methyl C–H bending (from 1470 to 1424 cm^{-1}) from cerebroside alone to MnO_2NPs (cerebroside) was indicative of a coordinative interaction between MnO_2 and cerebroside (Hazarika et al. 2017).

The HRTEM, SEM images, SAED pattern and EDX spectrum of MnO_2NPs (cerebroside) are presented in Fig. 7. The HRTEM images show layered nanosheets surrounding small spherical nanoparticles, similar to previous findings (Chen and Luan 2017). At high magnification (Fig. 7b and c), a combination of nanospheres and nanosheets was clearly visible. The size of MnO_2 nanospheres ranged from 6.99 to 16.57 nm (Fig. 7a–c). MnO_2 nanosheets are stacked layers of edge-sharing MnO_6 octahedra with water molecules and K^+ between the layers to balance the charge (Wang et al. 2017).

The SEM image also confirmed the presence of the interconnected nanosheets of MnO_2NPs (cerebroside) (Fig. 7d). The EDX spectrum confirmed the presence of Mn (56%) as well as oxygen (30%) and carbon (6%) from cerebroside (Fig. 7e). The presence of a potassium peak was also evident. The SAED pattern indicated polycrystalline material (Fig. 7a inset). The interplanar spacings of 0.245 nm and 0.142 nm corresponded to (110) and (020) planes, respectively, of δ-MnO_2 (birnessite) (Chen et al. 2017). The MnO_6 octahedra connect via edges in two dimensions forming sheets (Birgisson et al. 2018).

Antimicrobial activity

The antimicrobial activity of the plant extract, cerebroside and synthesized NPs was determined by measuring the zone of inhibition. No antimicrobial activity was observed for the plant extract, cerebroside and any of the MnO_2NPs. Table 1 shows the zones of inhibition of AgNPs synthesized using the plant extract and the positive control, ampicillin, against *E. faecalis*, *E. coli*, *K. pneumoniae* and *S. aureus*. An increase in the concentration (volume) of the AgNPs resulted in an increase in antimicrobial activity, which was consistent with previous studies (Guzman et al. 2012; Perni et al. 2013; Logeswari et al. 2015). AgNPs had comparable inhibitory action to ampicillin against *E. faecalis* ATCC 29212, but lower inhibition against *E. coli* ATCC 25922 and *S. aureus* ATCC 29213. Though ampicillin had no inhibitory action against *E. coli* ATCC 35218, *K. pneumoniae* ATCC 700603 and *S. aureus* ATCC 43300, AgNPs exhibited considerable activity at 40 µL. Due to the smaller size, shape and higher surface charge of AgNPs, they can attach and penetrate the cell membrane of the microorganisms. The AgNPs can then interact with the sulfur and phosphorus containing compounds, thereby causing damage to bacterial cells by interacting with the DNA, leading to cell death (Sangaonkar and Pawar 2018). This study shows that AgNPs

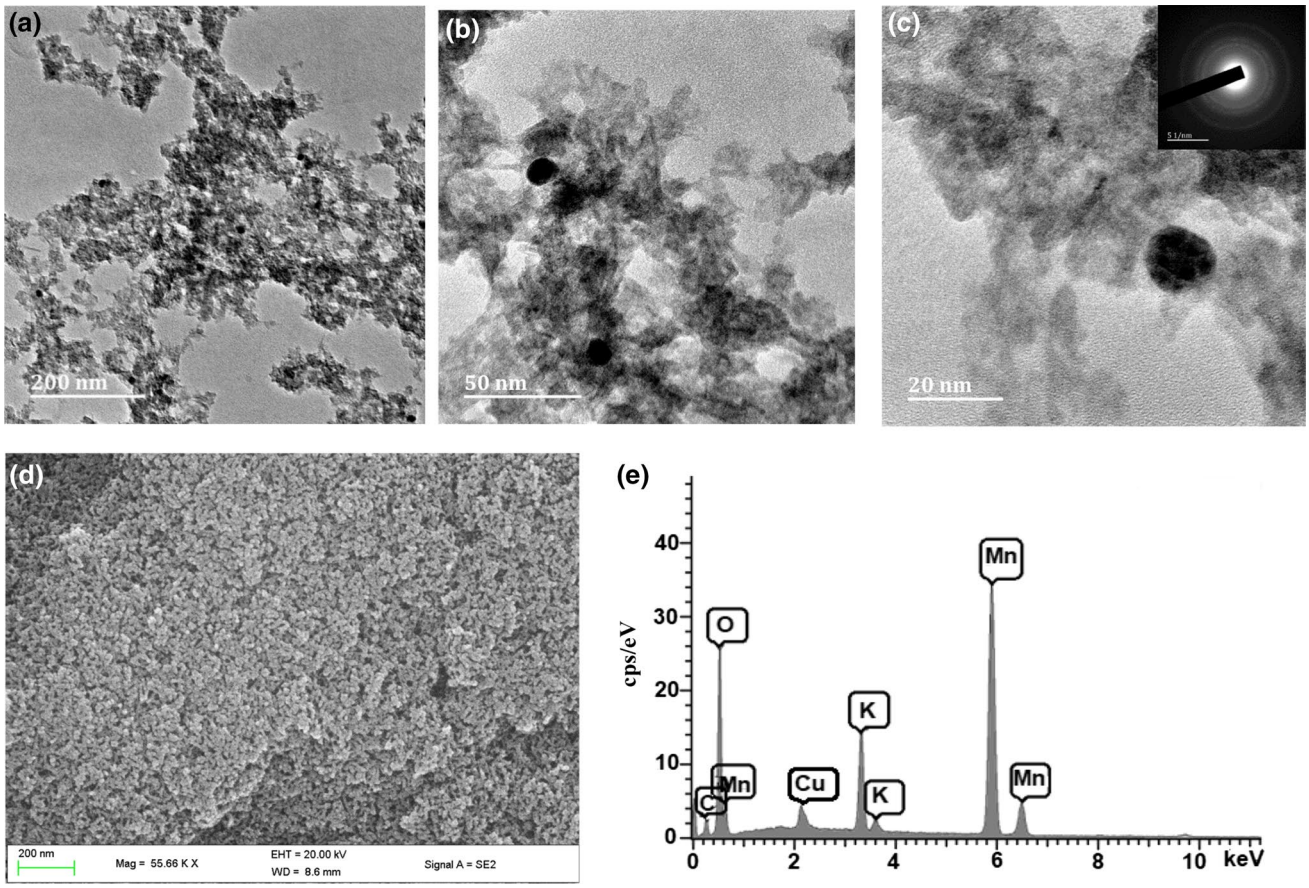

Fig. 7 HRTEM images (at different magnifications: **a** 200 nm, **b** 50 nm and **c** 20 nm) and corresponding SAED pattern (**c** inset), **d** SEM image and **e** EDX spectrum of MnO_2NPs (cerebroside)

Table 1 Zones of inhibition (in mm) of AgNPs synthesized using the extract of *C. zuluensis* (mean ± SD) and ampicillin against *E. faecalis*, *E. coli*, *K. pneumoniae* and *S.aureus*

	Zone of inhibition/mm		
	AgNPs (extract)		Ampicillin
	20 µL	40 µL	(10 µg per disk)
Enteroccocus faecali ATCC 29212	12 ± 0.6	16 ± 1.5	19
Escherichia coli ATCC 25922	10 ± 0.6	12 ± 0.6	22
Escherichia coli ATCC 35218	5 ± 0.6	10 ± 0.6	0
Klebsiella pneumoniae ATCC 700603	0	12 ± 1.5	0
Staphylococcus aureus ATCC 29213	0	11 ± 0.6	21
Staphylococcus aureus ATCC 43300	0	13 ± 1	0

capped with the biomolecules from the plant extract are most active against *E. faecalis* and *E. coli*, even at low concentrations. Previous studies have shown freestanding AgNPs as well as *C. zuluensis* to have no significant antimicrobial activity against *E. coli*, similar to this study (Tetyana et al. 2002). This suggests that the biogenic synthesis of AgNPs using *C. zuluensis* increases the antimicrobial potential of both *C. zuluensis* and AgNPs, thereby confirming a synergistic effect.

Antioxidant activity

The antioxidant capacity was determined by the DPPH radical scavenging activity (Fig. 8), ferric reducing antioxidant power (Fig. 9) and phosphomolybdenum activity for *C. zuluensis*, cerebroside and the NPs.

The DPPH radical scavenging activity was observed to be concentration dependent. Ascorbic acid and α-tocopherol had high DPPH radical scavenging ability and were therefore

omitted from the figure, for clarity. The radical scavenging activity was found to be in decreasing order of ascorbic acid > α-tocopherol > BHT > MnO_2NPs (extract) > MnO_2NPs (cerebroside) > AgNPs (extract) > extract > cerebroside. The ferric reducing antioxidant power (ability to reduce Fe(III) to Fe(II) ions by donor electrons) was found to be in decreasing order of cerebroside > BHT ~ extract > α-tocopherol > ascorbic acid > MnO_2NPs (cerebroside) > MnO_2NPs (extract) > AgNPs (extract). The results show the plant extract and its isolate to be better than the controls for reducing power, but not antioxidant power. When the extract was more active than cerebroside, which was least active for radical scavenging activity, MnO_2NPs synthesized by the extract were more active than those synthesized by cerebroside. Conversely, when cerebroside, which was most active in reducing power, was more active than the extract, MnO_2NPs synthesized by cerebroside was more active than those synthesized by the extract.

Previous studies have shown morphology and type of phytochemicals adsorbed onto MnO_2NPs to affect radical scavenging ability (Sivanesan et al. 2017). Similarly, our study shows that the phytocompounds adsorbed onto MnO_2NPs, by the plant-mediated synthesis route, influence its antioxidant potential, indicating that the capping agent is crucial for activity. MnO_2NPs (extract) was found to have better antioxidant activity than AgNPs (extract), which could be the result of the size and higher surface area of MnO_2NPs (Sivanesan et al. 2017).

The total antioxidant activity was also determined by the phosphomolybdenum method, which showed antioxidant activity to be in decreasing order of extract > α-tocopherol > ascorbic acid > cerebroside > BHT > AgNPs (extract) ~ MnO_2NPs (extract) > MnO_2NPs (cerebroside), again confirming that the activity is influenced by the synthesizing biomolecules.

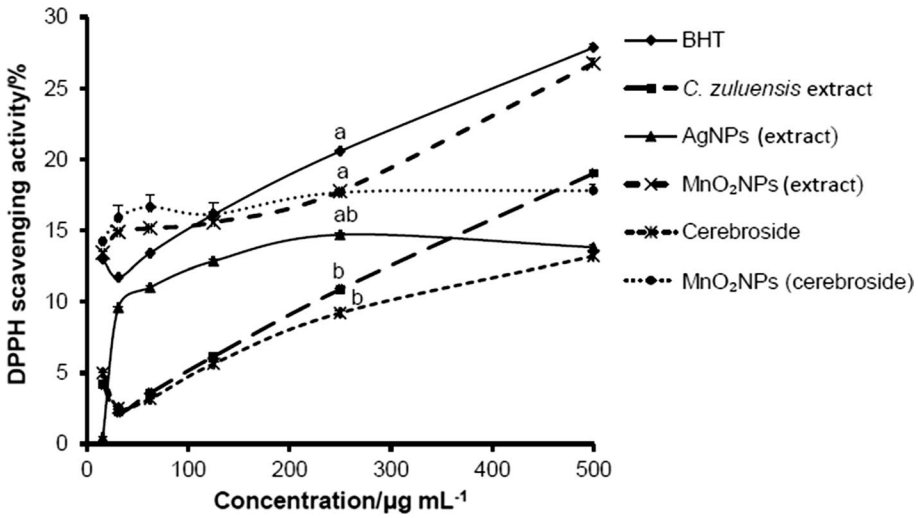

Fig. 8 DPPH radical scavenging activity of *C. zuluensis*, AgNPs, MnO_2NPs, cerebroside and MnO_2NPs (cerebroside). Values represented as mean ± SD, $n = 3$, different letters on graph indicate mean separation by Tukey post hoc test ($p < 0.05$)

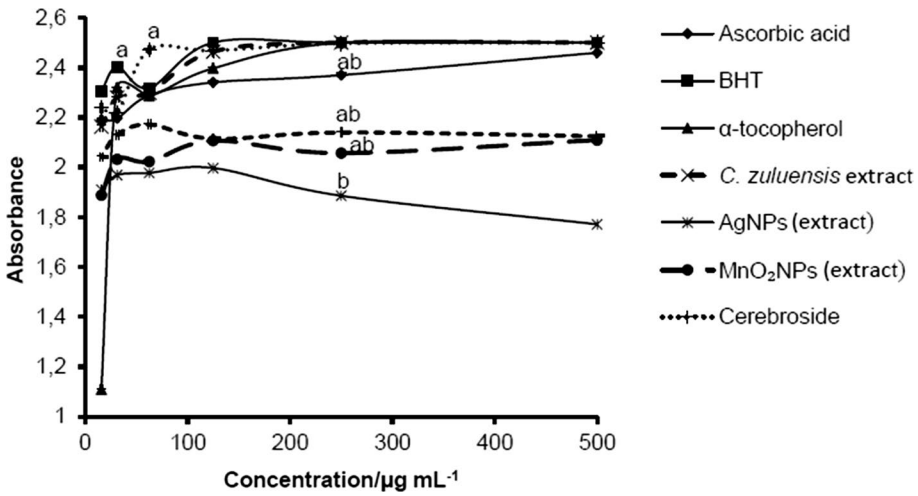

Fig. 9 Ferric reducing power of *C. zuluensis*, AgNPs, MnO_2NPs, cerebroside and MnO_2NPs (cerebroside) at 700 nm. Values represented as mean ± SD, $n = 3$, different letters

Conclusions

In this study, AgNPs and MnO_2NPs were successfully synthesized by the plant-mediated synthesis route, using the extract and pure isolate (aralia cerebroside) from *C. zuluensis*. AgNPs (extract) presented as spheres that were polydispersed with an average particle size of 7.43 nm and a layer of thin film surrounding the AgNPs, confirming the capping by biomolecules. The size and morphology of nanoparticles were influenced by the capping agent as seen with MnO_2NPs capped with biomolecules from the extract that presented as ultrathin nanoflakes with grainy morphology ranging from 11 to 29 nm, and MnO_2NPs capped with cerebroside that presented as nanospheres surrounded by nanosheets ranging from 6.99 to 16.57 nm. AgNPs showed better antimicrobial activity than MnO_2NPs and were most active against *Escherichia coli* and *Enterococcus faecalis*, while MnO_2NPs had better antioxidant activity than AgNPs. In all cases for MnO_2NPs, the results showed the capping biomolecules to affect the antioxidant capacity of the NPs, thereby confirming the importance of choice of plant material.

Acknowledgements The authors acknowledge the Microscopy and Microanalysis Unit, Instrumental Laboratory, NMR Unit, and UKZN Nanotechnology Platform, UKZN. This research was funded, in part, by the National Research Foundation through Dr Roshila Moodley (14008) and Dr Nomfundo T Mahlangeni (106490).

Compliance with ethical standards

Conflict of interest The authors declare that there is no conflict of interest.

References

Ahmed Y, Rahman S, Akthar P, Islam F, Rahman M, Yaakob Z (2013) Isolation of steroids from *n*-hexane extract of the leaves of *Saurauia roxburghii*. Int Food Res J 20:2939–2943

Ahmed S, Saifullah Ahmad M, Swami BL, Ikram S (2016) Green synthesis of silver nanoparticles using *Azadirachta indica* aqueous leaf extract. J Radiat Res Appl Sci 9:1–7. https://doi.org/10.1016/j.jrras.2015.06.006

Athar T, Topnani N, Hakeem A, Ahmed W (2012) Synthesis and characterization of MnO_2 and CdO nanoparticles. Adv Sci Lett 7:39–42. https://doi.org/10.1166/asl.2012.2191

Bayoudh A, Etteyeb N, Sediri F (2016) Hydrothermal synthesis, physico-chemical characterization and electrochemical behavior of β-MnO2 nanorods. Am J Nanosci 2:1–7. https://doi.org/10.11648/j.ajn.20160201.11

Birgisson S, Saha D, Iversen B (2018) Formation mechanisms of nanocrystalline MnO_2 polymorphs under hydrothermal conditions. Cryst Growth Des 18:827–838. https://doi.org/10.1021/acs.cgd.7b01304

Chen L, Luan G (2017) Morphology control of MnO_2 nanoparticles: effect of P123 polymer in ethanol-water system. Chem Ind Chem Eng Q 23:245–249. https://doi.org/10.2298/ciceq160316038c

Chen X, Yan S, Wang N, Peng S, Wang C, Hong Q, Zhang X, Dai S (2017) Facile synthesis and characterization of ultrathin delta-MnO_2 nanoflakes. RSC Adv 7:55734–55740. https://doi.org/10.1039/C7RA08962G

Cherian E, Rajan A, Baskar G (2016) Synthesis of manganese dioxide nanoparticles using co-precipitation method and its antimicrobial activity. Int J Mod Sci Technol 1:17–22

Corra S, Shoshan M, Wennemers H (2017) Peptide mediated formation of noble metal nanoparticles—controlling size and spatial arrangement. Curr Opin Chem Biol 40:138–144. https://doi.org/10.1016/j.cbpa.2017.09.005

De Villiers BJ, Van Vuuren SF, Van Zyl RL, Van Wyk BE (2010) Antimicrobial and antimalarial activity of *Cussonia* species (*Araliaceae*). J Ethnopharmacol 129:189–196. https://doi.org/10.1016/j.jep.2010.02.014

Deljou A, Goudarzi S (2016) Green extracellular synthesis of the silver nanoparticles using thermophilic *Bacillus* Sp. AZ1 and its antimicrobial activity against several human pathogenetic bacteria. Iran J Biotechnol 14:25–32. https://doi.org/10.15171/ijb.1259

Demirbas A, Büyükbezirci K, Celik C, Kislakci E, Karaagac Z, Gokturk E, Kati A, Cimen B, Yilmaz V, Ocsoy I (2019) Synthesis of long-term stable gold nanoparticles benefiting from red raspberry (*Rubus idaeus*), strawberry (*Fragaria ananassa*), and blackberry (*Rubus fruticosus*) extracts – gold ion complexation and investigation of reaction conditions. ACS Omega 4:18637–18644. https://doi.org/10.1021/acsomega.9b02469

Dogru E, Demirbas A, Altinsoy B, Duman F, Ocsoy I (2017) Formation of *Matricaria chamomilla* extract-incorporated Ag nanoparticles and size-dependent enhanced antimicrobial property. J Photochem Photobiol B 174:78–83. https://doi.org/10.1016/j.jphotobiol.2017.07.024

Ebede GR, Ndongo JT, Mbing JN, Kenfack HCM, Pegnyemb DE, Bochet CG (2019) Contortamide, a new anti-colon cancer cerebroside and other constituents from *Tabernaemontana contorta* Stapf (*Apocynaceae*). Nat Prod Res. https://doi.org/10.1080/14786419.2019.1636243

Elgorban A, El-Samawaty A, Yassin M, Sayed S, Adil S, Elhindi K, Bakri M, Khan M (2016) Antifungal silver nanoparticles: synthesis, characterization and biological evaluation. Biotechnol Biotechnol Equip 30:56–62. https://doi.org/10.1080/13102818.2015.1106339

Guilger-Casagrande M, Germano-Costa T, Pasquoto-Stigliani T, Fraceto L, de Lima R (2019) Biosynthesis of silver nanoparticles employing *Trichoderma harzianum* with enzymatic stimulation for the control of *Sclerotinia sclerotiorum*. Sci Rep 9:1–9. https://doi.org/10.1038/s41598-019-50871-0

Guzman M, Dille J, Godet S (2012) Synthesis and antibacterial activity of silver nanoparticles against gram-positive and gram-negative bacteria. Nanomedicine 8:37–45. https://doi.org/10.1016/j.nano.2011.05.007

Haneefa MM, Jayandran M, Balasubramanian V (2017) Green synthesis characterization and antimicrobial activity evaluation of manganese oxide nanoparticles and comparative studies with salicylalchitosan functionalized nanoform. Asian J Pharm 11:65–74. https://doi.org/10.22377/ajp.v11i01.1045

Hankey A (2005) Cussonia transvaalensis Reyneke. pza.sanbi.org/cussonia-transvaalensis%0D. Accessed 18 Jul 2019

Hazarika M, Borah D, Bora P, Silva A, Das P (2017) Biogenic synthesis of palladium nanoparticles and their applications as catalyst and antimicrobial agent. PLoS ONE 12:1–19. https://doi.org/10.1371/journal.pone.0184936

Hoseinpour V, Souri M, Ghaemi N (2018) Green synthesis, characterisation, and photocatalytic activity of manganese dioxide nanoparticles. Micro Nano Lett 13:1560–1563. https://doi.org/10.1049/mnl.2018.5008

Iravani S (2011) Green synthesis of metal nanoparticles using plants. Green Chem 13:2638–2650. https://doi.org/10.1039/c1gc15386b

Jaganyi D, Altaf M, Wekesa I (2013) Synthesis and characterization of whisker-shaped MnO_2 nanostructure at room temperature. Appl Nanosci 3:329–333. https://doi.org/10.1007/s13204-012-0135-3

Joshi N, Joshi E, Singh A (2020) Biological synthesis, characterisations and antimicrobial activities of manganese dioxide (MnO_2) nanoparticles. Res J Pharm Technol 13:135–140. https://doi.org/10.5958/0974-360X.2020.00027.X

Julin S, Nummelin S, Kostiainen M, Linko V (2018) DNA nanostructure-directed assembly of metal nanoparticle superlattices. J Nanopart Res 20:1–11. https://doi.org/10.1007/s11051-018-4225-3

Kaczmarek H, Metzler M, Wegrzynowska-Drzymalska K (2016) Effect of stabilizer type on the physicochemical properties of poly (acrylic acid)/silver nanocomposites for biomedical applications. Polym Bull 73:2927–2945. https://doi.org/10.1007/s00289-016-1617-3

Kang SS, Kim JS, Xu YN, Kim YH (1999) Isolation of a new cerebroside from the root bark of *Aralia elata*. J Nat Prod 62:1059–1060. https://doi.org/10.1021/np990018r

Kedi P, Meva E, Kotsedi L, Nguemfo E, Ntoumba A, Ahmed N, Mohamed Dongmo A, Maaza M (2018) Eco-friendly synthesis, characterization, in vitro and in vivo anti-inflammatory activity of silver nanoparticle-mediated *Selaginella myosurus* aqueous extract. Int J Nanomed 13:8537–8548. https://doi.org/10.2147/IJN.S174530

Khan MZH, Tareq FK, Hossen MA, Roki MNAM (2018) Green synthesis and characterization of silver nanoparticles using *Coriandrum savitum* leaf extract. J Eng Sci Technol 13:158–166

Khatun M, Billah M, Quader A (2012) Sterols and sterol glucoside from *Phyllanthus* species. Dhaka Univ J Sci 60:5–10. https://doi.org/10.3329/dujs.v60i1.10327

Kumar BMP, Shivaprasad KH, Raveendra RS, Krishna RH, Karikkat S, Nagabhushana BM (2014) Preparation of MnO_2 nanoparticles for the adsorption of environmentally hazardous malachite green dye. Int J Appl Innov Eng Manag 3:102–106

Lee JM, Lee DG, Lee KH, Cho SH, Nam K, Lee S (2013) Isolation and identification of phytochemical constituents from the fruits of *Acanthopanax senticosus*. Afr J Pharm Pharmacol 7:294–301. https://doi.org/10.5897/AJPP12.898

Leng Y, Fu L, Li B, Xu X, Xing X, He J, Song Y, Leng C, Guo Y, Ji X, Lu Z (2016) Protein-directed synthesis of highly monodispersed, spherical gold nanoparticles and their applications in multidimensional sensing. Sci Rep 6:1–11. https://doi.org/10.1038/srep28900

Ling T, Xia T, Wan X, Li D, Wei X (2006) Cerebrosides from the roots of *Serratula chinensis*. Molecules 11:677–683. https://doi.org/10.3390/11090677

Liu Z, Xu K, Sun H, Yin S (2015) One-step synthesis of single-layer MnO_2 nanosheets with multi-role sodium dodecyl sulfate for high-performance pseudocapacitors. Small 11:2182–2191. https://doi.org/10.1002/smll.201402222

Logeswari P, Silambarasan S, Abraham J (2015) Synthesis of silver nanoparticles using plants extract and analysis of their antimicrobial property. J Saudi Chem Soc 19:311–317. https://doi.org/10.1016/j.jscs.2012.04.007

Loo Y, Rukayadi Y, Nor-Khaizura M, Kuan C, Chieng B, Nishibuchi M, Radu S (2018) In vitro antimicrobial activity of green synthesized silver nanoparticles against selected gram-negative foodborne pathogens. Front Microbiol 9:1–7. https://doi.org/10.3389/fmicb.2018.01555

Loza K, Epple M (2018) Silver nanoparticles in complex media: an easy procedure to discriminate between metallic silver nanoparticles, reprecipitated silver chloride, and dissolved silver species. RSC Adv 8:24386–24391. https://doi.org/10.1039/C8RA04500C

Luo Y (2007) Preparation of MnO2 nanoparticles by directly mixing potassium permanganate and polyelectrolyte aqueous solutions. Mater Lett 61:1893–1895. https://doi.org/10.1016/j.matlet.2006.07.165

Makarov VV, Love AJ, Sinitsyna OV, Makarova SS, Yaminsky IV, Taliansky ME, Kalinina NO (2014) "Green" nanotechnologies: synthesis of metal nanoparticles using plants. Acta Naturae 6:35–44. https://doi.org/10.4135/9781452231631.n3

Malik P, Shankar R, Malik V, Sharma N, Mukherjee TK (2014) Green chemistry based benign routes for nanoparticle synthesis. J Nanoparticles 2014:1–14. https://doi.org/10.1155/2014/302429

Moon J-H, Munakata H, Kajihara K, Kanamura K (2013) Hydrothermal synthesis of manganese dioxide nanoparticles as cathode material for rechargeable batteries. Electrochemistry 81:2–6. https://doi.org/10.5796/electrochemistry.81.2

Moon SA, Salunke BK, Alkotaini B, Sathiyamoorthi E, Beom Soo K (2015) Biological synthesis of manganese dioxide nanoparticles by *Kalopanax pictus* plant extract. IET Nanobiotechnol 9:220–225. https://doi.org/10.1049/iet-nbt.2014.0051

Nasrollahzadeh M, Yek S, Motahharifar N, Gorab M (2019) Recent developments in the plant-mediated green synthesis of Ag-based nanoparticles for environmental and catalytic applications. Chem Rec 19:1–45. https://doi.org/10.1002/tcr.201800202

Nitie-Kang F, Onguéne PA, Lifongo LL, Ndom JC, Sippl W, Mbaze LM (2014) The potential of anti-malarial compounds derived from African medicinal plants, part II: a pharmacological evaluation of non-alkaloids and non-terpenoids. Malar J 13:1–20. https://doi.org/10.1186/1475-2875-13-81

Ocsy I, Demirbas A, McLamore E, Altinsoy B, Ildiz N, Baldemir A (2017) Green synthesis with incorporated hydrothermal approaches for silver nanoparticles formation and enhanced antimicrobial activity against bacterial and fungal pathogens. J Mol Liq 238:263–269. https://doi.org/10.1016/j.molliq.2017.05.012

Oladimeji AO, Oladosu IA, Jabeen A, Faheem A, Mesaik MA, Ali MS (2017) Immunomodulatory activities of isolated compounds from the root-bark of *Cussonia arborea*. Pharm Biol 55:2240–2247. https://doi.org/10.1080/13880209.2017.1400078

Parveen K, Banse V, Ledwani L (2016) Green synthesis of nanoparticles: Their advantages and disadvantages. In: Sharma NN, Gaol FL, Akthar J (eds) 2nd International Conference on Emerging Technologies: Micro to Nano 2015 (ETMN-2015). AIP Publishing, Rajasthan, pp 1–7

Perni S, Hakala V, Prokopovich P (2013) Biogenic synthesis of antimicrobial silver nanoparticles capped with L-cysteine. Colloids Surf A 460:219–224. https://doi.org/10.1016/j.colsurfa.2013.09.034

Saeed N, Khan MR, Shabbir M (2012) Antioxidant activity, total phenolic and total flavonoid contents of whole plant extracts *Torilis leptophylla* L. BMC Complement Altern Med 12:1–12. https://doi.org/10.1186/1472-6882-12-221

Sana S, Dogiparthi L (2018) Green synthesis of silver nanoparticles using *Givotia moluccana* leaf extract and evaluation of their antimicrobial activity. Mater Lett 226:47–51. https://doi.org/10.1016/j.matlet.2018.05.009

Sangaonkar GM, Pawar KD (2018) *Garcinia indica* mediated biogenic synthesis of silver nanoparticles with antibacterial and antioxidant activities. Colloids Surf B Biointerfaces 164:210–217. https://doi.org/10.1016/j.colsurfb.2018.01.044

Seoudi R, Shabaka A, El Sayed ZA, Anis B (2011) Effect of stabilizing agent on the morphology and optical properties of silver nanoparticles. Phys E Low-Dimens Syst Nanostruct 44:440–447. https://doi.org/10.1016/j.physe.2011.09.018

Shaabani A, Tavasoli-Rad F, Lee D (2005) Potassium permanganate oxidation of organic compounds. Synth Commun 35:571–580. https://doi.org/10.1081/SCC-200049792

Shen B, Linko V, Tapio K, Pikker S, Lemma T, Gopinath A, Gothelf K, Kostiainen M, Toppari J (2018) Plasmonic nanostructures through DNA-assisted lithography. Sci Adv 4:1–7. https://doi.org/10.1126/sciadv.aap8978

Singh A, Kaur K (2019) Biological and physical applications of silver nanoparticles with emerging trends of green synthesis. In: Silver Nanoparticles-Health and Safety. IntechOpen, pp 1–25. https://doi.org/10.5772/intechopen.88684

Sivanesan K, Jayakrishnan P, Razack SA, Sellaperumal P, Ramakrishnan G, Sahadevan R (2017) Biofabrication of manganese nanoparticle using *Aegle marmelos* fruit extract and assessment of its biological actvities. Nanomed Res J 2:171–178. https://doi.org/10.22034/nmrj.2017.03.005

Some S, Bulut O, Biswas K, Kumar A, Roy A, Sen K, Mandal A, Franco O, Ince I, Neog K, Das S, Pradhan S, Dutta S, Bhattacharjya D, Saha S, Mohapatra P, Bhuimali A, Unni B, Kati A, Mandal A, Yilmaz M, Ocsoy I (2019) Effect of feed supplementation with biosynthesized silver nanoparticles using leaf extract of Morus indica L. V1 on Bombyx mori L. (*Lepidoptera: Bombycidae*). Sci Rep 9:1–13. https://doi.org/10.1038/s41598-019-50906-6

Tetyana P, Prozesky EA, Jäger AK, Meyer JJM, van Staden J (2002) Some medicinal properties of *Cussonia* and *Schefflera* species used in traditional medicine. South Afr J Bot 68:51–54. https://doi.org/10.1016/S0254-6299(16)30454-9

Wang H, Lu Z, Qian D, Li Y, Zhang W (2007) Single-crystal α-MnO_2 nanorods: synthesis and electrochemical properties. Nanotechnology 18:115616. https://doi.org/10.1088/0957-4484/18/11/115616

Wang M, Zhang L, Huang W, Zhou Y, Zhao H, Lv J, Tian J, Kan X, Shi J (2017) Pt/MnO_2 nanosheets: facile synthesis and highly efficient catalyst for ethylene oxidation at low temperature. RSC Adv 7:14809–14815. https://doi.org/10.1039/c6ra26529d

Zhai T, Wang F, Yu M, Xie M, Liang C, Li C, Xiao F, Tang R, Wu Q, Lu X, Tong Y (2013) 3D MnO_2–graphene composites with large areal capacitance for high-performance asymmetric supercapacitors. Nanoscale 5:6790–6796. https://doi.org/10.1039/c3nr01589k

Zheng R, Xu X, Tian Z, Yang J (2009) Chemical constituents from the fruits of *Hippophae rhamnoides*. Nat Prod Res 23:1451–1456. https://doi.org/10.1080/14786410903075457